Opto-Electronic Science

Original Article

2022, Vol. 1, No. 4

DOI: 10.29026/oes.2022.210005

Charge carrier dynamics in different crystal phases of $CH_3NH_3PbI_3$ perovskite

Efthymis Serpetzoglou[1*], Ioannis Konidakis[1], George Kourmoulakis[1,3], Ioanna Demeridou[1,4], Konstantinos Chatzimanolis[2], Christos Zervos[2], George Kioseoglou[1,3], Emmanuel Kymakis[2] and Emmanuel Stratakis[1,3,4*]

Despite that organic-inorganic lead halide perovskites have attracted enormous scientific attention for energy conversion applications over the recent years, the influence of temperature and the type of the employed hole transport layer (HTL) on the charge carrier dynamics and recombination processes in perovskite photovoltaic devices is still largely unexplored. In particular, significant knowledge is missing on how these crucial parameters for radiative and non-radiative recombinations, as well as for efficient charge extraction vary among different perovskite crystalline phases that are induced by temperature variation. Herein, we perform micro photoluminescence (μPL) and ultrafast time resolved transient absorption spectroscopy (TAS) in Glass/Perovskite and two different Glass/ITO/HTL/Perovskite configurations at temperatures below room temperature, in order to probe the charge carrier dynamics of different perovskite crystalline phases, while considering also the effect of the employed HTL polymer. Namely, $CH_3NH_3PbI_3$ films were deposited on Glass, PEDOT:PSS and PTAA polymers, and the developed Glass/$CH_3NH_3PbI_3$ and Glass/ITO/HTL/$CH_3NH_3PbI_3$ architectures were studied from 85 K up to 215 K in order to explore the charge extraction dynamics of the $CH_3NH_3PbI_3$ orthorhombic and tetragonal crystalline phases. It is observed an unusual blueshift of the bandgap with temperature and the dual emission at temperature below of 100 K and also, that the charge carrier dynamics, as expressed by hole injection times and free carrier recombination rates, are strongly depended on the actual pervoskite crystal phase, as well as, from the selected hole transport material.

Keywords: transient absorption spectroscopy; μ-photoluminescence; variable temperature; perovskite crystalline phases; hole transport layer; charge carrier dynamics

Serpetzoglou E, Konidakis I, Kourmoulakis G, Demeridou I, Chatzimanolis K et al. Charge carrier dynamics in different crystal phases of $CH_3NH_3PbI_3$ perovskite. *Opto-Electron Sci* **1**, 210005 (2022).

Introduction

Organic-inorganic lead halide perovskites have attracted scientific attention during the last decades. Their extraordinary properties made them, one of the major competitors for next-generation optoelectronic applications, such as photovoltaics[1–3], light-emitting devices[1], photodetectors[4,5], random lasers[6], and light-emitting diodes[7,8]. In particular, the power conversion efficiency (PCE) of lead halide perovskite solar cells (PSCs) has been increased from ~4% up to 26.7% within a decade or

[1]Institute of Electronic Structure and Laser (IESL), Foundation for Research and Technology-Hellas (FORTH), Herakleio 70013, Greece; [2]Electrical and Computer Engineering Department, Hellenic Mediterranean University, Herakleio 71004, Greece; [3]Department of Materials Science and Technology, University of Crete, Herakleio 70013, Greece; [4]Department of Physics, University of Crete, Herakleio 70013, Greece.
*Correspondence: E Serpetzoglou, E-mail: eserpe@iesl.forth.gr; E Stratakis, E-mail: stratak@iesl.forth.gr
Received: 6 April 2021; Accepted: 19 August 2021; Published online: 21 April 2022

so[9–12]. This notable evolution of the efficiency of the perovskite solar cells are among other reasons due to the long-range electron and hole diffusion lengths in the perovskite layer, spontaneous exciton dissociation and tunable bandgap[13,14]. Despite the impressive increase in the PCE, a very crucial and unexplored area remains the intraband transition (hot carrier cooling process) in the perovskite layer and the charge carrier dynamics within the different crystal phases that the $CH_3NH_3PbI_3$ can be transformed depending on temperature. There are many strategies for engineering slow hot carrier cooling of the lead halide perovskites[15–18], but the exploration of this process is out of the scope of this manuscript and, is limited by our pulse duration. For the latter, the understanding of this effect is extremely crucial for low temperature applications, such as the use of PSCs in satellites or in space stations and to have clear view of the behavior of the perovskite layer at these conditions.

In particular, the lattice of the $CH_3NH_3PbI_3$ is orthorhombic below 160 K, tetragonal from 160 K up to 327 K, and cubic above 327 K[19]. It is well known, that the methylammonium cations in the perovskite A-site, in the tetragonal and cubic phases, show free rotation, resulting in the increase in the dielectric function, while in the orthorhombic phase, the organic cations are not free to rotate[20,21]. This free rotation is attributed to exciton binding energy[22,23], charge carrier transport and recombination[22–30], and to intraband relaxation[16,31–35]. The open question is how all these structural parameters correlate with the charge extraction dynamics. Remarkably, it is demonstrated in previous studies that the charge extraction properties from the perovskite light absorbing film correlate directly with the PCE of the fabricated solar cell devices[33–39]. Based on the above, it will be of great importance to address the evolution of charge extraction dynamics with temperature variation, and among crystal phase changes, while taking into account the nature of the employed hole transport layer (HTL) substrate. The latter is considered of great importance as there is still a significant lack of understanding of how the HTL polymers affect the charge extraction processes and the recombination dynamics within the different crystalline phases of the perovskite layer. In a set of excellent recent studies at variable temperatures, Milot et al[30]. and Diroll[31] have investigated the charge carrier dynamics of perovskite films deposited on bare glass and thick sapphire substrates, however, without taking into account the influence of the HTL on the charge carrier dynamics, and thus, charge extraction from the perovskite film to the HTL, i.e. a critical process for PSC device performance.

In this work, the charge carrier dynamics of Glass/ITO/HTL/$CH_3NH_3PbI_3$ configurations are studied at variable temperatures by means of microphotoluminescence (μPL) and ultrafast time-resolved transient absorption spectroscopy (TAS), while using a typical glass as a reference substrate and two different types of HTL polymers for the sake of comparison. This approach allows us to explore how the different perovskite crystal phases, as well as, the employed HTL polymer affect the charge carrier dynamics, transport, and recombination rates within the developed architectures. In particular, the μPL emission of the perovskite is studied from 85 K up to 215 K in glass/perovskite configuration, while two types of HTL polymers were employed, i.e. the more hydrophilic and rough poly (3,4-ethylenedioxythiophene)-poly (styrenesulfonate), known as PEDOT: PSS (Fig. S1(a) and Fig. S2(a)), and the less hydrophilic and smoother poly (triarylamine) semiconductor, known as PTAA (Fig. S1(b) and Fig. S2(b)). It is well known that a very crucial parameter is to select the appropriate HTL film for the perovskite solar cells because it is vital to have a perfect interface for an efficient carrier extraction from the perovskite layer to the transport layer and the electrode. A key parameter for the selection of the HTL is the minimum energy difference between the work function (WF) of the HTL and the HOMO level of the perovskite, to have easier and more efficient hole injection from the perovskite layer to the HTL. Moreover, the hydrophilicity of the HTL is also an important parameter. If the HTL is hydrophobic, the drag force tension of the HTL to the perovskite will be decreased and thus, the crystallization of the perovskite layer will lead to larger grains size that are attributed to faster charge carrier dynamics, better electrical characteristics, and more efficient perovskite solar cell devices[33]. It was demonstrated recently, that upon using the latter polymer the quality of the perovskite film is enhanced (Fig. S1(d)), and consequently the photovoltaic performance of the fabricated PSCs improved significantly as an outcome of faster charge carrier dynamics and slower recombination processes, even though the crystal quality of the perovskite was similar for the studied configurations (Glass/$CH_3NH_3PbI_3$, PEDOT: PSS/$CH_3NH_3PbI_3$ and PTAA/$CH_3NH_3PbI_3$) (Fig. S1(e))[33]. However, it remains unknown and critical, if this holds throughout all crystalline phases of

$CH_3NH_3PbI_3$ at lower temperatures, or if that is solely the case for the tetragonal phase that exists at operating temperatures nearby room temperature.

Temperature dependent μPL

Figure 1(a–c) show the PL spectra of the studied Glass/$CH_3NH_3PbI_3$, Glass/ITO/PEDOT: PSS/$CH_3NH_3PbI_3$ and Glass/ITO/PTAA/$CH_3NH_3PbI_3$ architectures, as recorded from 85 K up to 215 K. It is necessary to mention that the intensity of PL peaks do not follow any trend, i.e. the intensity of the PL peak of the orthorhombic to decrease and of the tetragonal phase to increase as the temperature increases. This is a result of different roughness of the surface of the perovksite layer, as well as the inhomogeneous transform of the tetragonal phase to the orthorhombic phase and vice versa, as the PL measurements are performed in different spot into the perovskite layer in every temperature to prevent any degradation effect. The μPL spectra at 85 K exhibit two characteristic emission peaks, namely, for the orthorhombic phase and the tetragonal phase, located at 1.67 and 1.59 eV, respectively. The high-energy emission peak which is attributed to the orthorhombic phase exhibits blueshifts of ~ 7 meV (from 1.673 to 1.680 eV) for Glass/$CH_3NH_3PbI_3$, ~5 meV (from 1.668 to 1.673 eV) for Glass/ITO/PEDOT: PSS/$CH_3NH_3PbI_3$ and ~ 8 meV (from 1.674 to 1.682 eV) for Glass/ITO/PTAA/$CH_3NH_3PbI_3$, before disappearing above 120 K (Fig. 2(a–c) red solid circles).

The obtained bandgap widening of the high-energy peak, as extracted for the PL spectra, is in disagreement with the Varshni behavior of standard tetrahedral semiconductors, in which as the temperature increases the band-gap presents a redshift[41]. In addition, the low-energy emission peak which is attributed to the tetragonal phase exhibits redshifts of ~ 17 meV (from 1.592 to 1.575 eV) for Glass/$CH_3NH_3PbI_3$, ~ 16 meV (from 1.590 to 1.576 eV) for Glass/ITO/PEDOT: PSS/$CH_3NH_3PbI_3$ and ~ 19 meV (from 1.604 to 1.585 eV) for Glass/ITO/PTAA/$CH_3NH_3PbI_3$ as the temperature increases up to 120, 115 and 120 K, respectively. Then as the temperature increases further up to 215 K, exhibits blueshift of ~ 15 meV (from 1.575 to 1.590 eV) for Glass/$CH_3NH_3PbI_3$, ~ 14 meV (from 1.576 to 1.590 eV) for Glass/ITO/PEDOT: PSS/$CH_3NH_3PbI_3$ and ~11 meV (from 1.585 to 1.596 eV) for Glass/ITO/PTAA/$CH_3NH_3PbI_3$. It is also necessary to mention that the μPL behavior for the three studied architectures seems to be independent of the employed substrate (Glass) or the HTL polymer (PEDOT: PSS and PTAA). The origin of this unusual blue shift is due to the thermal expansion of the $CH_3NH_3PbI_3$ lattice. Therefore, the overlap between Pb-6s and I-5s antibonding atomic orbitals, forming the valence maximum, is reduced due to this expansion.

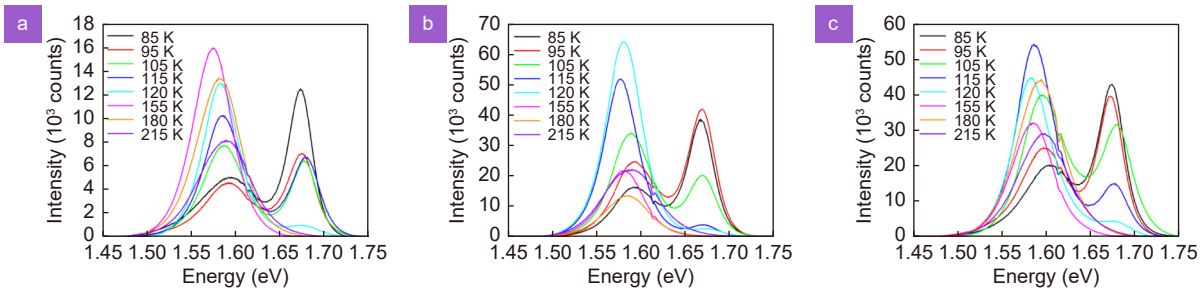

Fig. 1 | μPL spectra following excitation at 543 nm of the (**a**) Glass/$CH_3NH_3PbI_3$, (**b**) Glass/ITO/PEDOT:PSS/$CH_3NH_3PbI_3$ and (**c**) Glass/ITO/PTAA/$CH_3NH_3PbI_3$ architectures.

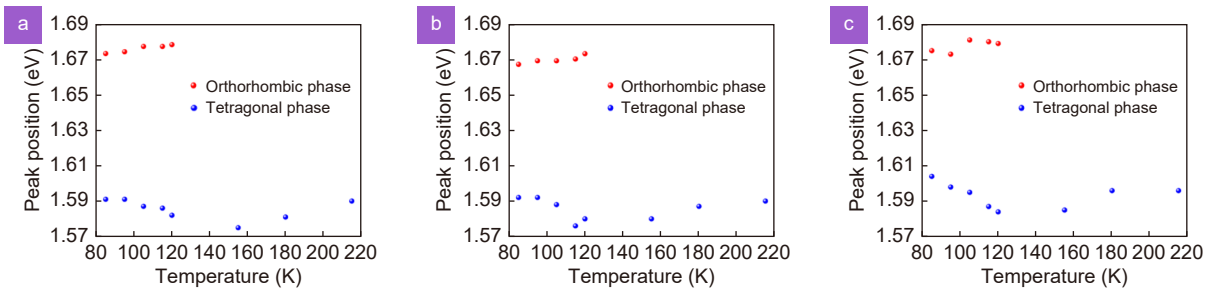

Fig. 2 | Shift of the μPL emission peak as a function of temperature for (**a**) Glass/$CH_3NH_3PbI_3$, (**b**) Glass/ITO/PEDOT:PSS/$CH_3NH_3PbI_3$ and (**c**) Glass/ITO/PTAA/$CH_3NH_3PbI_3$ architectures for the orthorhombic (red solid circles) and tetragonal (blue solid circles) perovskite crystal phases.

Figure 3 shows the evolution of the Full Width Half Maximum (FWHM) of the PL emission peaks for all studied architectures as extracted from the Fig. 1(a–c) and corresponds to the orthorhombic and tetragonal phases. We can fit our data by taking into account the temperature-independent inhomogeneous broadening (Γ_0) and the interaction between charge carriers and LO-phonons, described by Fröhlich Hamiltonian equation (Eq. (1))[42]:

$$\Gamma(T) = \Gamma_0 + \gamma_{AC} T + \gamma_{LO}/(\exp(E_{LO}/k_B T) - 1) \quad . \quad (1)$$

The extracted fitting set values (Γ_0, γ_{LO}, E_{LO}) are (17.7, 38.3, 8.82) meV for Glass/$CH_3NH_3PbI_3$, (19.8, 42.9, 9.47) meV for Glass/ITO/PEDOT: PSS/$CH_3NH_3PbI_3$ and (23.4, 31.0, 8.68) meV for Glass/ITO/PTAA/$CH_3NH_3PbI_3$. The extracted values for all studied architectures are in agreement with the values in the literature, even though the energy of the optical phonons in organic-inorganic perovskites is still unclear[42].

Moreover, the broadening of the PL spectra as the temperature increases is strongly correlated with the trap states. The energetics of the trap states are affected by the phase transition of the perovskite layer, which affects the alteration in electronic band structure that could lead to different energy band edges and trap levels[30]. As the temperature increases the mobility of the excited electron is lowered[43] and thus are unable to reach the non-radiative recombination centres (perovskite defects) and recombine radiatively. This poses a plausible explanation of the broadening of the PL FWHM as the temperature increases, while is in agreement with the slower τ_1 as extracted from the TAS findings, i.e. as thoroughly discussed in a later section. Namely, for both phases of Glass/ITO/PTAA/$CH_3NH_3PbI_3$ architecture and for the tetragonal phase of Glass/ITO/PEDOT: PSS/$CH_3NH_3PbI_3$ configuration. In the orthorhombic phase, for the latter configuration, the broadening of the FWHM as the temperature increases is in disagreement with τ_1, possibly due to the higher density of traps as a result of the hydrophilicity of the PEDOT: PSS polymer[33].

Furthermore, the origin of the dual emission peak is still controversial as one would expect the distinct PL signature of each phase to be absent within the temperature range that the other phase is dominant. However, similar findings as the ones of the present study are reported in the literature. Namely, Wehrenfennig et al. have already shown that phonon-interactions have a significant impact on the luminescence and charge transport properties of these perovskites[40,44]. Moreover, Phuong et al.[45], Xing et al.[6] and Fang et al.[46] have suggested that free and bound exciton generate high- and low- energy emission peaks. Kong et al.[47] acknowledged that the high-energy peak can be attributed to the transitions of the free-excitons, but he assigned the low-energy emission peak to the defects. Finally, Wehrenfennig et al.[48] ascribed the obtained two emission peaks to coexisting tetragonal inclusions and the orthorhombic matrix at the lower temperatures. We believe that for the temperature below of 120 K we can detect the orthorhombic and the tetragonal phases, as well, because of the trapped tetragonal phases in the low temperature orthorhombic phase.

Temperature dependent TAS

In order to extract useful information about the charge carrier dynamics at low temperatures and the so formed different crystal phases of the perovskite, we studied the Glass/ITO/PEDOT: PSS/$CH_3NH_3PbI_3$ and Glass/ITO/PTAA/$CH_3NH_3PbI_3$ architectures because the extraction of the holes to the glass on Glass/$CH_3NH_3PbI_3$ configuration is not possible. At this point, we have to mention that we studied the orthorhombic and tetragonal

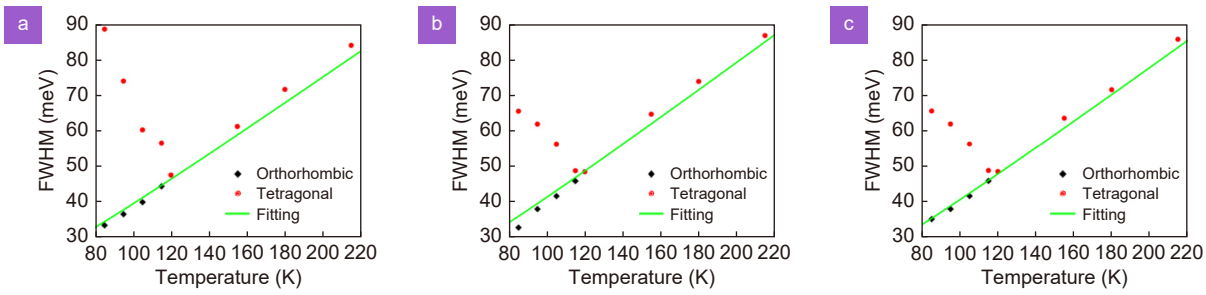

Fig. 3 | FWHM of the PL peaks corresponding to the orthorhombic (black diamonds) and tetragonal (red circles) phases of $CH_3NH_3PbI_3$ as a function of temperature (a) Glass/$CH_3NH_3PbI_3$, (b) Glass/ITO/PEDOT:PSS/$CH_3NH_3PbI_3$ and (c) Glass/ITO/PTAA/$CH_3NH_3PbI_3$. Green solid lines show the fitting acquired by the temperature-independent inhomogeneous broadening (Γ_0) and the interaction between charge carriers and longitudinal optical phonons (LO-phonons), as described by the Fröhlich Hamiltonian.

phase and not the cubic phase, because we have already explored the influence of the employed HTL polymers in the cubic phase in our previous publication[49]. Figure 4 and Fig. 5 display the typical TAS spectra of delta optical density (ΔOD) as a function of wavelength at various delay times, for Glass/ITO/PEDOT: PSS/$CH_3NH_3PbI_3$ and Glass/ITO/PTAA/$CH_3NH_3PbI_3$, configurations respectively (see Fig. S1), following photoexcitation at 1026 nm and a pump fluence of 1 mJ cm^{-2}. In order to exclude any degradation effect throughout the duration of experiments, samples of this study were placed in a handmade sealed holder with nitrogen for the room temperature TAS measurements. For the low temperature TAS and PL measurements were quickly transferred inside a commercially available cryostat and maintained under vacuum for the total duration of the experiment. However, upon using 1026 nm as a pump wavelength which results in two-photon absorption process, we were extremely cautious to minimize the undesired effects upon employing the minimal required fluence at 1026 nm.

The main ΔOD peaks at the vicinity of 735 nm (Fig. 4(a, b) and Fig. 5(a, b)) are attributed to the transient photo-induced bleaching of the band edge transition of the orthorhombic phase of $CH_3NH_3PbI_3$, while the corresponding peaks at ca. 760 nm (Fig. 4(b, c) and Fig. 5(b, c)) emerge due to the tetragonal phase. Meanwhile, a photo-induced transient absorption (PIA) in the range of 550–700 nm is additionally observed at all temperatures for both studied configurations.

We consider first the obtained shifts of the optical density (ΔOD) peaks at the zero-time delay (t=0 ps). Figure 6 shows the delta optical density (ΔOD) peaks wavelength at t = 0 ps as a function temperature for the studied architectures. It becomes apparent that both configurations exhibit similar trends for both orthorhombic and tetragonal phases. In particular, the peak wavelength of the orthorhombic phase drops from 737 nm to 730 nm for Glass/ITO/PEDOT: PSS/$CH_3NH_3PbI_3$ configuration and from 727 nm to 724 nm for Glass/ITO/PTAA/$CH_3NH_3PbI_3$ architecture, when the temperature increases from 85 K to 120 K. Notably, at 120 K both orthorhombic and tetragonal perovskite crystal phases coexist (Fig. 4(b) and Fig. 5(b)). This widening of the bandgap is in contrast with the Varshni behavior that standard tetrahedral semiconductors show, in which the bandgap presents a redshift with the increase in temperature[44,50]. However, in the present case the obtained blueshift, i.e. widening of the band gap, can be explained plausibly by the fact that upon cooling the perovskite below the transition temperature, the methylammonium (MA) cations could be kinetically trapped in disordered configurations in an ordered orthorhombic phase of $CH_3NH_3PbI_3$, resulting to lowering the bandgap of the perovskite layer[50,51].

Additionally, when the temperature increases further from 120 K to 155 K, the wavelength of the absorption

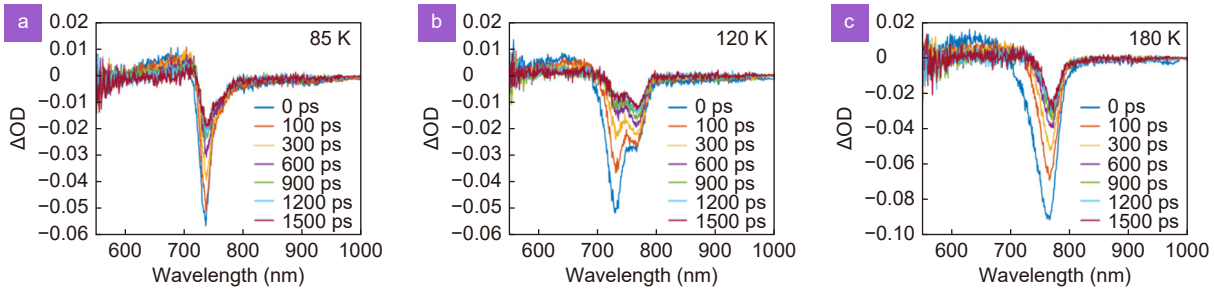

Fig. 4 | Optical density (ΔOD) vs. wavelength at various delay times for Glass/ITO/PEDOT:PSS/$CH_3NH_3PbI_3$ architecture at (**a**) 85 K, (**b**) 120 K and (**c**) 180 K.

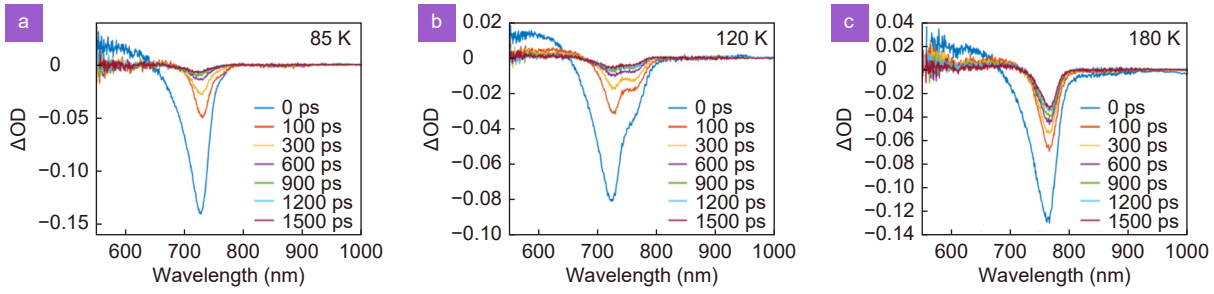

Fig. 5 | Optical density ΔOD vs. wavelength at various delay times for Glass/ITO/PTAA/$CH_3NH_3PbI_3$ configuration at (**a**) 85 K, (**b**) 120 K and (**c**) 180 K.

peak that is attributed to the tetragonal phase, shifts from 766 nm to 770 nm for the Glass/ITO/PEDOT: PSS/$CH_3NH_3PbI_3$ configuration, and from 760 nm to 767 nm for the Glass/ITO/PTAA/$CH_3NH_3PbI_3$ architecture. The obtained initial redshift is indicative of the change from the orthorhombic to the tetragonal phase and is a result of changes in methylammonium disorder and spin-orbit coupling[51–53]. Moreover, when the temperature increases from 155 K to 215 K, the absorption peak wavelength decreases from 770 nm to 757 nm for the first architecture, and from 767 nm to 753 nm for the latter. Dar et al.[50] have shown that the MA-ordered domains (T < transition temperature) have larger bandgap than the MA-disordered domains (at the tetragonal phase), which is in agreement with our experimental results (Fig. 6) when comparing the orthorhombic with the tetragonal phase[48]. Also, the obtained blueshift of the absorption peak in the tetragonal phase is rationalized due to the thermal expansion of the $CH_3NH_3PbI_3$ lattice[54].

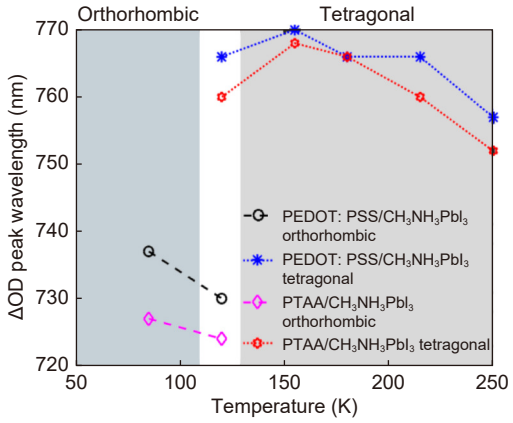

Fig. 6 | Optical density (ΔOD) peaks wavelength as a function of temperature for Glass/ITO/PEDOT:PSS/$CH_3NH_3PbI_3$ architecture and Glass/ITO/PTAA/$CH_3NH_3PbI_3$ configurations, as extracted from TAS spectra at t = 0 ps (see Fig. 4 and Fig. 5 blue lines).

In order to probe the charge extraction dynamics within the two HTL/perovskite architectures, we perform a fitting analysis, using the two well established models. Namely, a three-exponential fitting model allows us to determine critical time components of the charge carrier transport processes between the perovskite film and the employed hole transport layers[33–37,49,55,56]; The high-order polynomial model provides important kinetic rates for charge carrier recombination processes that occur within the perovskite film[35,38,39,57–62]. The first model is based on the equation $\Delta OD = A_1\exp(-t/\tau_1) + A_2\exp(-t/\tau_2) + A_3\exp(-t/\tau_3)$, and all kinetic parameters for the three studied temperatures, i.e. 85 K, 120 K and 180 K, are summarized in Table 1. Figure 7(a) and 7(b) show the three-exponential fittings for the orthorhombic phase, while Fig. 7(c) and 7(d) depict the corresponding fittings of the tetragonal phase for Glass/ITO/PEDOT:PSS/$CH_3NH_3PbI_3$ and Glass/ITO/PTAA/$CH_3NH_3PbI_3$ configurations. The insets of Fig. 7(a) and 7(d) have shown the initial time range of the Glass/ITO/PTAA/$CH_3NH_3PbI_3$ architecture, which looks like a vertical line in the full-time scale range, due to the fact that the carrier trapping and hole injection for this architecture are extremely fast.

Table 1 lists values of τ_1 time component, which represents the time for the charge carrier trapping at the perovskite grain boundaries and perovskite/HTL interfaces[33,49,57]. In the case of Glass/ITO/PEDOT: PSS/$CH_3NH_3PbI_3$, the τ_1 increases as the temperature rises for the orthorhombic phase, meaning that the trapping becomes slower and/or the density of the traps has increased and is in disagreement with the broadening of FWHM of the PL emission peaks. Furthermore, in the case of Glass/ITO/PTAA/$CH_3NH_3PbI_3$, the τ_1 is found to decrease slighter as the temperatures increases, which is in agreement with the broadening of the PL FWHM as has already discussed and also implies that it is less dependent on the perovskite crystal phase and the density of the traps. Moreover, at 120 K where the two phases coexist, it appears that in the case of the former configuration, the orthorhombic phase exhibits slightly faster trap filling. Once again, when the PTAA is employed, both phases show similar trap filling times. It has thus emerged, that when the more hydrophobic PTAA polymer is used as HTL material, the trap filling time remains mostly unaffected by the temperature variation, and thus, independent of the existing phase types.

The second-time component (τ_2) represents the time required for a hole injection from the perovskite film to the HTL polymer[33,49,57]. Inspection of Table 1 reveals that for both phases (orthorhombic at ~730 nm and tetragonal at ~760 nm) the hole injection time component (τ_2) decreases as the temperature increases. In particular, for the Glass/ITO/PEDOT:PSS/$CH_3NH_3PbI_3$ architecture in the orthorhombic phase, τ_2 decreases by almost a factor of three, from 562 ps to 171 ps, when the temperature increases from 85 K to 120 K. While, in the tetragonal phase, the hole injection time is reduced around two times from 449 ps to 266 ps, when the temperature rises further from 120 K to 180 K. Notably, similar trends are also observed in Glass/ITO/PTAA/$CH_3NH_3PbI_3$ configuration. For the peak of the orthorhombic phase, the τ_2

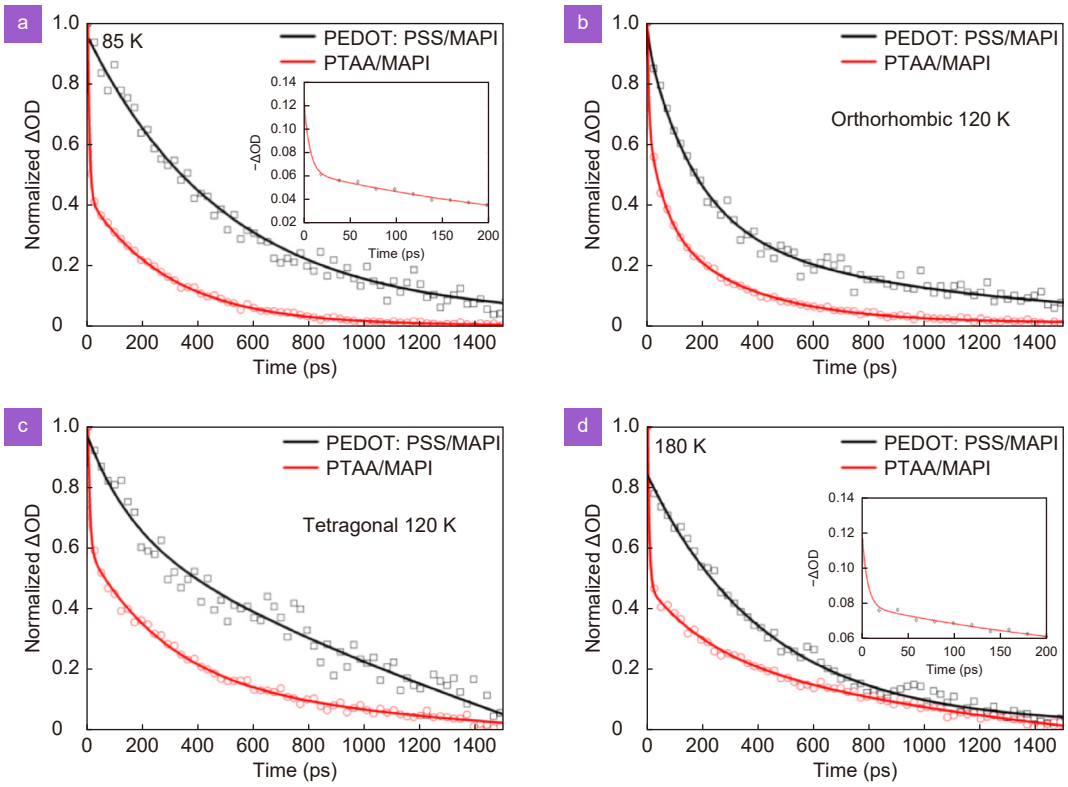

Fig. 7 | Normalized optical density (ΔOD) vs. delay time for Glass/ITO/PEDOT:PSS/$CH_3NH_3PbI_3$ and Glass/ITO/PTAA/$CH_3NH_3PbI_3$ configurations for the orthorhombic phase at (**a**) 85 K, (**b**) 120 K and for the tetragonal phase at (**c**) 120 K and (**d**) 180 K. Symbols present the transient band edge bleach kinetics, while solid lined present the decay exponential fitting. Insets are shown the initial time scale for Glass/ITO/PTAA/$CH_3NH_3PbI_3$.

Table 1 | Time components and bimolecular recombination rate (k_2) for the Glass/ITO/PEDOT:PSS/$CH_3NH_3PbI_3$ and Glass/ITO/PTAA/$CH_3NH_3PbI_3$ architectures.

Temperature (K)	PEDOT: PSS					PTAA				
	λ_{max} (nm)	$\tau_1 \pm 2$ (ps)	$\tau_2 \pm 8$ (ps)	$\tau_3 \pm 13$ (ps)	$k_2 \pm 0.2\times10^{-10}$ (cm^3s^{-1})	λ_{max} (nm)	$\tau_1 \pm 2$ (ps)	$\tau_2 \pm 8$ (ps)	$\tau_3 \pm 13$ (ps)	$k_2 \pm 0.2\times10^{-10}$ (cm^3s^{-1})
85	737	6.1	562	562	9.9×10^{-10}	727	6.2	296	296	9.1×10^{-10}
120	730	12	171	962	9.9×10^{-10}	724	5.7	64	324	3.8×10^{-10}
	766	16.7	449	995	1.3×10^{-9}	760	7.3	137	362	6.6×10^{-10}
180	752	14.7	266	933	1.2×10^{-10}	766	5.7	57	1839	1.0×10^{-10}

is decreased by a factor of five, from 296 ps to 64 ps, and for the tetragonal phase, the hole injection time is decreased by almost a factor of three, from 137 ps to 57 ps. These findings suggest that the hole injection for studied architectures in both crystal phases becomes faster and more efficient as the temperature increases.

Table 1 also lists the third-time component (τ_3), which is representative of the electron-hole recombination[33,49,57]. Table 1 reveals that τ_3 increases as the temperature rises, in the case of PTAA and for the orthorhombic phase in the case of PEDOT:PSS, meaning that the free carriers are available for longer periods in the perovskite film in order to approach the perovskite/HTL interface and inject into the transport layer polymer. While in the tetragonal phase in the case of PEDOT:PSS, τ_3 remains approximately constant, when the temperature increases from 120 K to 180 K, meaning that the τ_3 is unaffected by rising temperature.

The second fitting model that we used, is the high-order polynomial, based on equation

$$dn(t)/dt = -k_3n^3 - k_2n^2 - k_1n\ ,$$

where n is the charge carrier density, k_1, k_2 and k_3 indicate the rate constants corresponding respectively to, trap-assisted recombination, bimolecular recombination, and Auger trimolecular recombination processes[35,38,39,57,58–62]. In the present study, we focus on the k_2 parameter, as it is the one that is strongly related to

the performance of the devices and is the key component for this model as reported by Wehrenfennig et al.[39]. Table 1 includes the bimolecular recombination rate, k_2, and Fig. S6 shows the polynomial fittings for the orthorhombic phase (Fig. S6(a, b)) and for the tetragonal phase (Fig. S6(c, d)) for Glass/ITO/PEDOT: PSS/$CH_3NH_3PbI_3$ and Glass/ITO/PTAA/$CH_3NH_3PbI_3$ configurations. For the Glass/ITO/PEDOT: PSS/$CH_3NH_3PbI_3$ configuration, in the orthorhombic phase, k_2 is equal for both temperatures (85 K and 120 K) at 9.9×10^{-10} cm^3s^{-1}, while in the tetragonal phase it decreases by an order of magnitude, from 1.3×10^{-9} cm^3s^{-1} to 1.2×10^{-10} cm^3s^{-1}, as the temperature increases from 120 K to 180 K. Rather differently, in the orthorhombic phase of Glass/ITO/PTAA/$CH_3NH_3PbI_3$ architecture, k_2 is found to decrease from 9.1×10^{-10} cm^3s^{-1} to 3.8×10^{-10} cm^3s^{-1}, as the temperature rises from 85 K to 120 K, whereas in the tetragonal phase is decreased six times from 6.6×10^{-10} cm^3s^{-1} at 120 K to 1.0×10^{-10} cm^3s^{-1} at 180 K. Furthermore, another interesting observation from Table 1, reveals that the Glass/ITO/PTAA/$CH_3NH_3PbI_3$ architecture exhibits faster hole injection (τ_2) and slower bimolecular recombination rates (k_2) for all studied temperatures when compared to the Glass/ITO/PEDOT: PSS/$CH_3NH_3PbI_3$ configuration. Notably, these trends are in total agreement with our previously reported room temperature findings on the same architectures[30]. The first implies more efficient charge extraction from the perovskite to the HTL, while the latter is evidence of longer diffusion lengths of the free charge carriers within the perovskite film. Nevertheless, both of these factors are known to favor power conversion efficiency when it comes to PSC devices[33,39].

In particular, at room temperature, it was shown that the obtained shorter hole injection times and slower bimolecular recombination rates for PTAA samples, were correlated with the considerably larger crystal grains (Fig. S1(d)), and better energy alignment between the perovskite and the HTL[33]. Herein, we also observe that the effect of the temperature on the obtained dynamics is notable for both HTL configurations, in agreement with Milot et al.[28] where they have shown that the bimolecular recombination rate reduces as the temperature rises, as a result of electron-phonon interactions. In general, the bimolecular recombination rate (k_2) is expected to reduce with decreasing the charge-carrier mobility, because in affected by the average velocity of approach into the Coulomb capture radius. Based on the above, the present studies reveal that the influence of the employed hole transport layer, as well as the temperature induced phase transitions, are of equal significance for the hole injection dynamics, the bimolecular recombination rates, and thus, for the performance of PSC devices in which such HTL/perovskite configurations are employed.

Conclusion

By means of μPL and TAS, we monitor the charge carrier dynamics of $CH_3NH_3PbI_3$ films at low temperatures in order to extract useful information about the effect of the different crystal structures of the perovskite on the carrier dynamics. Moreover, the perovskite films were crystallized on the surface of the glass and two well-studied HTL polymers, the hydrophilic PEDOT:PSS and the more hydrophobic PTAA, in order to explore for the first time the effect of the HTL on the perovskite charge extraction properties at low temperatures. In particular, through the μPL measurements, it is observed an unusual blueshift of the bandgap with temperature which is in discord with the Varshni behavior of the typical semiconductor below 120 K for the orthorhombic phase of the perovskite and the dual emission at temperature below of 100 K. Moreover, in three studied temperatures by means of TAS, at 85 K (orthorhombic phase), at 120 K (coexistence of the orthorhombic and the tetragonal phase) for each peak, and at 180 K (tetragonal phase) the Glass/ITO/PTAA/$CH_3NH_3PbI_3$ architecture exhibits faster hole injection from the perovksite layer to the HTL and slower recombination rates (k_2) when compared with the Glass/ITO/PEDOT:PSS/$CH_3NH_3PbI_3$ configuration. Furthermore, as the temperature increases for each perovskite crystal phase (orthorhombic and tetragonal), the τ_2 time components and k_2 bimolecular recombination rate decrease, for both configurations. Thus, it was found that the charge carrier dynamics at low temperatures, are not only affected by the employed hole transport layer, as we have already shown for the room temperature measurements but are strongly correlated to the different perovskite crystal phases.

References

1. Stranks SD, Snaith HJ. Metal-halide perovskites for photovoltaic and light-emitting devices. *Nat Nanotechnol* **10**, 391–402 (2015).
2. Zhao XY, Deng WW. Printing photovoltaics by electrospray. *Opto-Electron Adv* **3**, 190038 (2020).
3. Wang YS, Arumugam GM, Mahmoudi T, Mai YH, Hahn YB et

al. A critical review of materials innovation and interface stabilization for efficient and stable perovskite photovoltaics. *Nano Energy* **87**, 106141 (2021).
4. Lee Y, Kwon J, Hwang E, Ra CH, Yoo WJ et al. High-performance perovskite-graphene hybrid photodetector. *Adv Mater* **27**, 41–46 (2015).
5. Wang F, Zou X, Xu M, Wang H, Wang H et al. Recent Progress on Electrical and Optical Manipulations of Perovskite Photodetectors. *Adv Sci* **8**, 2100569 (2021).
6. Xing GC, Mathews N, Lim SS, Yantara N, Liu XF et al. Low-temperature solution-processed wavelength-tunable perovskites for lasing. *Nat Mater* **13**, 476–480 (2014).
7. Tan ZK, Moghaddam RS, Lai ML, Docampo P, Higler R et al. Bright light-emitting diodes based on organometal halide perovskite. *Nat Nanotechnol* **9**, 687–692 (2014).
8. Li ZT, Cao K, Li JS, Tang Y, Ding XR et al. Review of blue perovskite light emitting diodes with optimization strategies for perovskite film and device structure. *Opto-Electron Adv* **4**, 200019 (2021).
9. Kojima A, Teshima K, Shirai Y, Miyasaka T. Organometal halide perovskites as visible-light sensitizers for photovoltaic cells. *J Am Chem Soc* **131**, 6050–6051 (2009).
10. Snaith HJ. Perovskites: the emergence of a new era for low-cost, high-efficiency solar cells. *J Phys Chem Lett* **4**, 3623–3630 (2013).
11. Gao P, Grätzel M, Nazeeruddin MK. Organohalide lead perovskites for photovoltaic applications. *Energy Environ Sci* **7**, 2448–2463 (2014).
12. NREL best research-cell photovoltaic efficiency chart. https://www.nrel.gov/pv/cell-efficiency.html
13. Xing GC, Mathews N, Sun SY, Lim SS, Lam YM et al. Long-range balanced electron-and hole-transport lengths in organic-inorganic $CH_3NH_3PbI_3$. *Science* **342**, 344–347 (2013).
14. Stranks SD, Eperon GE, Grancini G, Menelaou C, Alcocer MJP et al. Electron-hole diffusion lengths exceeding 1 micrometer in an organometal trihalide perovskite absorber. *Science* **342**, 341–344 (2013).
15. Nie ZH, Gao XZ, Ren YJ, Xia SY, Wang YH et al. Harnessing hot phonon bottleneck in metal halide perovskite nanocrystals via interfacial electron –phonon coupling. *Nano Lett* **20**, 4610–4617 (2020).
16. Chen JS, Messing ME, Zheng KB, Pullerits T. Cation-dependent hot carrier cooling in halide perovskite nanocrystals. *J Am Chem Soc* **141**, 3532–3540 (2019).
17. Chung H, Jung SI, Kim HJ, Cha W, Sim E et al. Composition-dependent hot carrier relaxation dynamics in cesium lead halide ($CsPbX_3$, X = Br and I) perovskite nanocrystals. *Angew Chem Int Ed* **56**, 4160–4164 (2017).
18. Protesescu L, Yakunin S, Bodnarchuk MI, Krieg F, Caputo R et al. Nanocrystals of cesium lead halide perovskites ($CsPbX_3$, X = Cl, Br, and I): novel optoelectronic materials showing bright emission with wide color gamut. *Nano Lett* **15**, 3692–3696 (2015).
19. Liu YC, Yang Z, Liu SZ. Recent progress in single-crystalline perovskite research including crystal preparation, property evaluation, and applications. *Adv Sci* **5**, 1700471 (2018).
20. Poglitsch A, Weber D. Dynamic disorder in methylammoniumtrihalogenoplumbates (II) observed by millimeter-wave spectroscopy. *J Chem Phys* **87**, 6373–6378 (1987).
21. Wasylishen RE, Knop O, Macdonald JB. Cation rotation in methylammonium lead halides. *Solid State Commun* **56**, 581–582 (1985).
22. Even J, Pedesseau L, Katan C. Analysis of multivalley and multibandgap absorption and enhancement of free carriers related to exciton screening in hybrid perovskites. *J Phys Chem C* **118**, 11566–11572 (2014).
23. D'Innocenzo V, Grancini G, Alcocer MJP, Kandada ARS, Stranks SD et al. Excitons versus free charges in organo-lead tri-halide perovskites. *Nat Commun* **5**, 3586 (2014).
24. Yi HT, Wu XX, Zhu XY, Podzorov V. Intrinsic charge transport across phase transitions in hybrid organo-inorganic perovskites. *Adv Mater* **28**, 6509–6514 (2016).
25. Chin XY, Cortecchia D, Yin J, Bruno A, Soci C. Lead iodide perovskite light-emitting field-effect transistor. *Nat Commun* **6**, 7383 (2015).
26. Biewald A, Giesbrecht N, Bein T, Docampo P, Hartschuh A et al. Temperature-dependent ambipolar charge carrier mobility in large-crystal hybrid halide perovskite thin films. *ACS Appl Mater Interfaces* **11**, 20838–20844 (2019).
27. Etienne T, Mosconi E, De Angelis F. Dynamical origin of the rashba effect in organohalide lead perovskites: a key to suppressed carrier recombination in perovskite solar cells. *J Phys Chem Lett* **7**, 1638–1645 (2016).
28. Eperon GE, Jedlicka E, Ginger DS. Biexciton auger recombination differs in hybrid and inorganic halide perovskite quantum dots. *J Phys Chem Lett* **9**, 104–109 (2018).
29. Zhu HM, Trinh MT, Wang J, Fu YP, Joshi PP et al. Organic cations might not be essential to the remarkable properties of band edge carriers in lead halide perovskites. *Adv Mater* **29**, 1603072 (2017).
30. Milot RL, Eperon GE, Snaith HJ, Johnston MB, Herz LM. Temperature-dependent charge-carrier dynamics in $CH_3NH_3PbI_3$ perovskite thin films. *Adv Funct Mater* **25**, 6218–6227 (2015).
31. Diroll BT. Temperature-dependent intraband relaxation of hybrid perovskites. *J Phys Chem Lett* **10**, 5623–5628 (2019).
32. Zhu HM, Miyata K, Fu YP, Wang J, Joshi PP, Niesner D et al. Screening in crystalline liquids protects energetic carriers in hybrid perovskites. *Science* **353**, 1409–1413 (2016).
33. Serpetzoglou E, Konidakis I, Kakavelakis G, Maksudov T, Kymakis E et al. Improved carrier transport in perovskite solar cells probed by femtosecond transient absorption spectroscopy. *ACS Appl Mater Interfaces* **9**, 43910–43919 (2017).
34. Kakavelakis G, Maksudov T, Konios D, Paradisanos I, Kioseoglou G et al. Efficient and highly air stable planar inverted perovskite solar cells with reduced graphene oxide doped PCBM electron transporting layer. *Adv Energy Mater* **7**, 1602120 (2016).
35. Ishioka K, Barker BG Jr, Yanagida M, Shirai Y, Miyano K. Direct observation of ultrafast hole injection from lead halide perovskite by differential transient transmission spectroscopy. *J Phys Chem Lett* **8**, 3902–3907 (2017).
36. Zhu ZL, Ma JN, Wang ZL, Mu C, Fan ZT et al. Efficiency enhancement of perovskite solar cells through fast electron extraction: the role of graphene quantum dots. *J Am Chem Soc* **136**, 3760–3763 (2014).
37. Corani A, Li MH, Shen PS, Chen P, Guo TF et al. Ultrafast dynamics of hole injection and recombination in organometal halide perovskite using nickel oxide as p-type contact electrode. *J Phys Chem Lett* **7**, 1096–1101 (2016).
38. Draguta S, Christians JA, Morozov YV, Mucunzi A, Manser JS

et al. A quantitative and spatially resolved analysis of the performance-bottleneck in high efficiency, planar hybrid perovskite solar cells. *Energy Environ Sci* **11**, 960–969 (2018).
39. Wehrenfennig C, Eperon GE, Johnston MB, Snaith HJ, Herz LM. High charge carrier mobilities and lifetimes in organolead trihalide perovskites. *Adv Mater* **26**, 1584–1589 (2014).
40. Wehrenfennig C, Liu MZ, Snaith HJ, Johnston MB, Herz LM. Homogeneous emission line broadening in the organo lead halide perovskite $CH_3NH_3PbI_{3-x}Cl_x$. *J Phys Chem Lett* **5**, 1300–1306 (2014).
41. Varshni YP. Temperature dependence of the energy gap in semiconductors. *Physica* **34**, 149–154 (1967).
42. Wright AD, Verdi C, Milot RL, Eperon GE, Pérez-Osorio MA et al. Electron–phonon coupling in hybrid lead halide perovskites. *Nat Commun* **7**, 11755 (2016).
43. Ma J, Wang LW. The nature of electron mobility in hybrid perovskite $CH_3NH_3PbI_3$. *Nano Lett* **17**, 3646–3654 (2017).
44. Wehrenfennig C, Liu MZ, Snaith HJ, Johnston MB, Herz LM. Charge-carrier dynamics in vapour-deposited films of the organolead halide perovskite $CH_3NH_3PbI_{3-x}Cl_x$. *Energy Environ Sci* **7**, 2269–2275 (2014).
45. Phuong LQ, Nakaike Y, Wakamiya A, Kanemitsu, Y. Free excitons and exciton–phonon coupling in $CH_3NH_3PbI_3$ single crystals revealed by photocurrent and photoluminescence measurements at low temperatures. *J Phys Chem Lett* **7**, 4905–4910 (2016).
46. Fang HH, Raissa R, Abdu - Aguye M, Adjokatse S, Blake GR et al. Photophysics of organic–inorganic hybrid lead iodide perovskite single crystals. *Adv Funct Mater* **25**, 2378–2385 (2015).
47. Kong WG, Ye ZY, Qi Z, Zhang BP, Wang M et al. Characterization of an abnormal photoluminescence behavior upon crystal-phase transition of perovskite $CH_3NH_3PbI_3$. *Phys Chem Chem Phys* **17**, 16405–16411 (2015).
48. Wehrenfennig C, Liu MZ, Snaith HJ, Johnston MB, Herz LM. Charge carrier recombination channels in the low-temperature phase of organic-inorganic lead halide perovskite thin films. *APL Mater* **2**, 081513 (2014).
49. Serpetzoglou E, Konidakis I, Maksudov T, Panagiotopoulos A, Kymakis E et al. *In situ* monitoring of the charge carrier dynamics of $CH_3NH_3PbI_3$ perovskite crystallization process. *J Mater Chem C* **7**, 12170–12179 (2019).
50. Dar MI, Jacopin G, Meloni S, Mattoni A, Arora N et al. Origin of unusual bandgap shift and dual emission in organic-inorganic lead halide perovskites. *Sci Adv* **2**, e1601156 (2016).
51. Baikie T, Fang YN, Kadro JM, Schreyer M, Wei FX et al. Synthesis and crystal chemistry of the hybrid perovskite $(CH_3NH_3)PbI_3$ for solid-state sensitised solar cell applications. *J Mater Chem A* **1**, 5628–5641 (2013).
52. Even J, Pedesseau L, Katan C, Kepenekian M, Lauret JS et al. Solid-state physics perspective on hybrid perovskite semiconductors. *J Phys Chem C* **119**, 10161–10177 (2015).
53. Even J, Pedesseau L, Jancu JM, Katan C. DFT and *k•p* modelling of the phase transitions of lead and tin halide perovskites for photovoltaic cells. *Phys Status Solidi RRL* **8**, 31–35 (2014).
54. Filippetti A, Delugas P, Saba MI, Mattoni A. Entropy-suppressed ferroelectricity in hybrid lead-iodide perovskites. *J Phys Chem Lett* **6**, 4909–4915 (2015).
55. Ghosh T, Aharon S, Etgar L, Ruhman S. Free carrier emergence and onset of electron–phonon coupling in methylammonium lead halide perovskite films. *J Am Chem Soc* **139**, 18262–18270 (2017).
56. Zhai YX, Sheng CX, Zhang C, Vardeny ZV. Ultrafast spectroscopy of photoexcitations in organometal trihalide perovskites. *Adv Funct Mater* **26**, 1617–1627 (2016).
57. Konidakis I, Maksudov T, Serpetzoglou E, Kakavelakis G, Kymakis E et al. Improved charge carrier dynamics of $CH_3NH_3PbI_3$ perovskite films synthesized by means of laser- assisted crystallization. *ACS Appl Energy Mater* **1**, 5101–5111 (2018).
58. Klein JR, Flender O, Scholz M, Oum K, Lenzer T. Charge carrier dynamics of methylammonium lead iodide: from PbI_2-rich to low-dimensional broadly emitting perovskites. *Phys Chem Chem Phys* **18**, 10800–10808 (2016).
59. Manser JS, Kamat PV. Band filling with free charge carriers in organometal halide perovskites. *Nat Photon* **8**, 737–743 (2014).
60. Stranks SD, Burlakov VM, Leijtens T, Ball JM, Goriely A et al. Recombination kinetics in organic-inorganic perovskites: excitons, free charge, and subgap states. *Phys Rev Appl* **2**, 034007 (2014).
61. Piatkowski P, Cohen B, Ramos FJ, Di Nunzio M, Nazeeruddin MK et al. Direct monitoring of ultrafast electron and hole dynamics in perovskite solar cells. *Phys Chem Chem Phys* **17**, 14674–14684 (2015).
62. La-o-vorakiat C, Salim T, Kadro J, Khuc MT, Haselsberger R et al. Elucidating the role of disorder and free-carrier recombination kinetics in $CH_3NH_3PbI_3$ perovskite films. *Nat Commun* **6**, 7903 (2015).

Acknowledgements

This research has been cofinanced by the European Regional Development Fund of the European Union and Greek national funds through the Operational Program Competitiveness, Entrepreneurship and Innovation, under the call RESEARCH – CREATE – INNOVATE (project code:T1EDK-01082). IK also acknowledges HELLAS-CH (MIS 5002735) Implemented under "Action for Strengthening Research and Innovation Infrastructures", funded by the Operational Programme"Competitiveness, Entrepreneurship and Innovation" (NSRF 2014-2020) and co-financed by Greece and the European Union (European Regional Development Fund).

Competing interests

The authors declare no competing financial interests.

Supplementary information

Experimental details of the developed glass/perovskite and HTL/perovskite architectures, μPL and TAS setup, error analysis for the exponential fitting model, characterization of materials (AFM and contact angle of HTLs), SEM images, transient band edge bleach kinetics and their corresponding decay polynomial fits (lines) and error analysis for the exponential fitting model.

Supplementary information for this paper is available at https://doi.org/10.29026/oes.2022.210005